ACS OMEGA

http://pubs.acs.org/journal/acsodf

Article

Exploring the Complex Interplay of Anisotropies in Magnetosomes of Magnetotactic Bacteria

David Gandia, Lourdes Marcano, Lucía Gandarias, Alicia G. Gubieda, Ana García-Prieto, Luis Fernández Barquín, Jose Ignacio Espeso, Elizabeth Martín Jefremovas, Iñaki Orue, Ana Abad Diaz de Cerio, Mª Luisa Fdez-Gubieda,* and Javier Alonso*

Cite This: *ACS Omega* 2025, 10, 16061−16072

Read Online

ACCESS | Metrics & More | Article Recommendations | Supporting Information

ABSTRACT: Magnetotactic bacteria (MTB) are at the forefront of interest for biophysics applications, especially in cancer treatment. Magnetosomes biomineralized by these bacteria are high-quality magnetic nanoparticles that form chains inside the MTB through a highly reproducible, naturally driven process. In particular, *Magnetovibrio blakemorei* and *Magnetospirillum gryphiswaldense* MTB exhibit distinct magnetosome morphologies: truncated hexa-octahedral and cuboctahedral shapes, respectively. Despite having identical compositions (magnetite, Fe_3O_4) and dimensions within a similar size range, their effective uniaxial anisotropies significantly differ at room temperature, with *M. blakemorei* exhibiting ∼25 kJ/m^3 and *M. gryphiswaldense* ∼ 11 kJ/m^3. This prominent anisotropy variance provides a unique opportunity to explore the role of magnetic anisotropy contributions in the magnetic responses of these magnetite-based nanoparticles. This study systematically investigates these responses by examining static magnetization as a function of temperature (M vs T, 5 mT) and magnetic field (M vs $\mu_0 H$, up to 1 T). Above the Verwey transition temperature (∼110 K), the effective anisotropy is dominated by the shape anisotropy contribution, notably increasing the coercivity for *M. blakemorei* by up to twofold compared to *M. gryphiswaldense*. However, below this temperature, the effective uniaxial anisotropy rapidly increases in a nonmonotonic way, significantly changing the magnetic behavior. Computational simulations using a dynamic Stoner−Wohlfarth model provide insights into these phenomena, enabling careful interpretation of experimental data. According to our simulations, below the Verwey temperature, a uniaxial magnetocrystalline contribution progressively emerges, peaking around 22−24 kJ/m^3 at 5 K. Our study reveals the complex evolution of magnetocrystalline contributions, which dominate the magnetic response of magnetosomes below the Verwey temperature. This demonstrates the profound impact of anisotropic properties on the magnetic behaviors and applications of magnetite-based nanoparticles and highlights the exceptional utility of magnetosomes as ideal model systems for studying the complex interplay of anisotropies in magnetite-based nanoparticles.

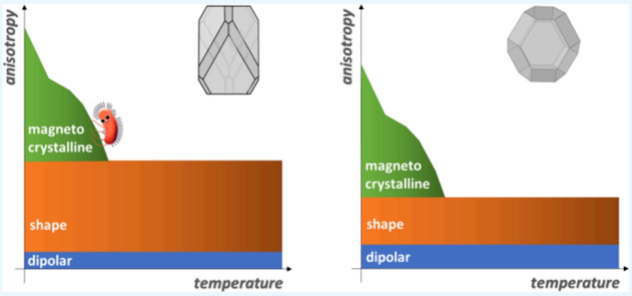

1. INTRODUCTION

Magnetotactic bacteria (MTB) are unique aquatic microorganisms capable of directional movement guided by Earth's magnetic field.[1−3] This remarkable ability is due to the presence of intracellular magnetosomes. The latter are magnetic nanoparticles enclosed in a lipid bilayer, which tend to form chains inside the MTB, and are predominantly composed of magnetite (Fe_3O_4). Interestingly, these nanoparticles demonstrate a high degree of chemical purity and uniformity in size (35−120 nm), achieved through a naturally driven biomineralization process that ensures reproducibility and magnetic stability of the magnetosomes at room temperature.[4,5]

Recent years have witnessed burgeoning interest in MTB, mainly driven by the potential of magnetosomes in various biomedical applications, such as magnetic hyperthermia and magnetic resonance imaging (MRI), and by the possibility of using MTB as remotely controlled microrobots.[6−23] Beyond their practical applications, magnetosomes serve as excellent subjects for fundamental nanomagnetic studies due to their consistent composition, size, shape, and arrangement. This precision allows them to model nanomagnetic phenomena, like the influence of dipolar interactions in one-dimensional assemblies or the effect of particle morphology on magnetic response at the nanoscale.[24−27] To this respect, our previous research utilized experimental techniques and computational methods to highlight the significant role of particle shape in

Received: October 14, 2024
Revised: February 10, 2025
Accepted: February 13, 2025
Published: April 14, 2025

determining the magnetic properties of faceted magnetosomes, specifically those synthesized by *M. gryphiswaldense*.[26] These studies revealed that magnetosomes from this species presented a slight deformation, which tilted the magnetic moment out of the chain easy axis and allowed to accommodate the chain to the characteristic helical morphology of these bacteria. This deformation in the cuboctahedral shape of these magnetosomes crucially influence their magnetic response and heating efficiency in therapeutic applications like magnetic hyperthermia.[28]

However, leveraging magnetosomes as model systems presents challenges, primarily because their morphology, governed by genetic factors, is species specific and not readily modifiable like synthetic nanoparticles.[29−33] The diversity of MTB species and their magnetosome morphologies is vast, yet culturing these organisms in a laboratory setting remains a significant hurdle,[34−37] limiting most research to a few species like *Magnetospirillum gryphiswaldense* MSR-1 and *Magnetospirillum magneticum* AMB-1.[38,39]

This study goes a step beyond by culturing and determining the anisotropy variations in *Magnetovibrio blakemorei* strain MV-1, which produces elongated Fe_3O_4 magnetosomes with a distinct truncated hexa-octahedral shape. This allows for a direct comparison of the magnetic properties with *M. gryphiswaldense*. First isolated by Bazylinski et al. in 1988,[40] *M. blakemorei* has been less studied due to the challenges associated with its cultivation.[1,41−44]

This work presents a detailed analysis of the magnetic properties of *M. blakemorei*, comparing them with those of *M. gryphiswaldense*. Both species synthesize high-quality Fe_3O_4 magnetosomes with comparable sizes but different shapes. Our experiments, conducted with the magnetosomes intact within the bacteria, allow precise control over magnetic interactions and external conditions, enabling us to simulate and compare their magnetic responses under various temperatures. Utilizing experimental measurements focused on the collection of hysteresis loops across a wide range of temperatures (5 to 300 K), along with calculations based on a dynamic Stoner−Wohlfarth model, the thermal evolution of their magnetic anisotropies has been dissected, providing invaluable insights into the fundamental magnetic parameters that govern the behavior of magnetite-based nanoparticles of biotechnological interest. This study not only advances our understanding of MTB but also underscores the significance of magnetosomes as ideal model systems in nanomagnetic research, potentially benefiting various applications in the field of magnetic nanoparticles, not only restricted to biomedicine but also expanding to emergent fields, like topological spin textures or bioencoded magnonics.[45]

2. METHODS

2.1. Magnetotactic Bacterial Culture. *Magnetospirillum gryphiswaldense* MSR-1 (DMSZ 6631) was grown without shaking at 28 °C in flask standard medium using 0.3% (wt/vol) of sodium pyruvate as carbon source and supplemented with 100 μM of Fe(III)-citrate.[46] Bacteria were grown in bottles with a headspace-to-liquid ratio of 1:4, and an inoculum of 10% was used to start the cultures. Under these conditions, we have observed that the oxygen concentration in the liquid drops to microaerophilic levels within an hour, which is optimal for magnetosome formation by *M. gryphiswaldense*. *M. blakemorei* strain MV-1 (DSM 18854) was grown at 30 °C in liquid medium containing per liter of artificial seawater (ASW): 4 g of Na succinate × $6H_2O$, 0.8 g of Na acetate, 1 g of casamino acids (BD BACTO), 1 g of NH_4Cl, 5 mL of Wolfe's mineral solution, and 50 μL of 1%(w/v) resazurin. After autoclaving, 0.5 mL of BME Vitamins 100× solution (Sigma-Aldrich, B6891), 1.8 mL of 0.5 M PO_4 buffer, 0.3 mL of Fe(II)-Cl_2, and 10 mL of 0.25 M freshly made cysteine solution were added to the media and the pH was adjusted to 7. The media were then distributed into sterile Hungate tubes and fluxed for 20 min with N_2O, which is the final electron acceptor used by *M. blakemorei* and provides an anaerobic atmosphere optimal for magnetosome synthesis by this strain. Once bacteria present well-formed magnetosome chains, and the cells were harvested by centrifugation, fixed with 2% glutaraldehyde, washed three times with PBS, and finally suspended in Milli-Q water.

2.2. Transmission Electron Microscopy. Transmission electron microscopy (TEM) was carried out on whole bacteria (i.e., whole cells) deposited onto 300 mesh carbon-coated copper grids. The images were obtained with a JEOL JEM-1400Plus electron microscope at an accelerating voltage of 120 kV. The particle size and morphology were analyzed with ImageJ software.[47] The crystallographic planes and dimensions were estimated by analyzing the 2D projections of magnetosomes in different orientations and comparing them with those expected for an ideal truncated hexa-octahedral (for *M. blakemorei*) or cuboctahedral (for *M. gryphiswaldense*) structure.

2.3. Magnetic Measurements. Magnetic measurements were performed in a superconducting quantum interference device magnetometer (Quantum Design MPMS-5). The magnetic characterization was carried out using the whole bacteria. The samples were freeze-dried and encapsulated in gelatin capsules. The gelatin capsules containing the powdered samples were placed inside a plastic straw, which was then attached to the sample rod and inserted into the magnetometer. The magnetic signal from the gelatin capsule, straw, and sample rod is diamagnetic and is negligible compared to that of the sample. The magnetic signal from the bacterial body is also diamagnetic but non-negligible at high fields and therefore was subtracted from the final magnetic measurements. Magnetization vs temperature (M vs T) curves were measured following the usual zero-field-cooling/field-cooling (ZFC/FC) protocol, with an applied magnetic field of 5 mT. Magnetization vs magnetic field (M vs μ_0H) loops were measured in both ZFC and FC modes at different temperatures, 5−300 K, applying magnetic fields, μ_0H, up to 1 T. Field-cooled M vs μ_0H measurements were carried out by cooling the sample under a 1 T field to each individual target temperature in separate runs.

2.4. Computational Simulations. Computational simulations are based on a dynamic Stoner−Wohlfarth model that has been described before in detail in previous studies.[48,49] Each magnetosome in the chain is considered as a single domain magnetic moment. For a given magnetic field at a fixed temperature, the equilibrium configuration of these magnetic moments is calculated by minimizing the single dipole energy density, given as the sum of three contributions: (i) the effective cubic anisotropy energy density (E_{cub}), due to the magnetocrystalline anisotropy above T_v and the small cubic contribution to the shape anisotropy for *M. gryphiswaldense*; (ii) the effective uniaxial anisotropy energy density (E_{uni}), arising from the competition between magnetosome shape anisotropy and dipolar interactions within the chain (across all

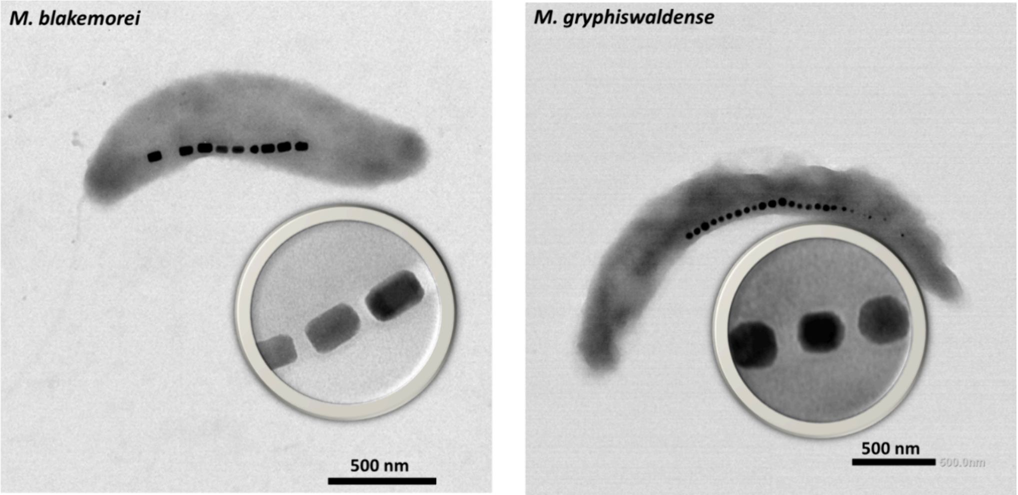

Figure 1. TEM images of the *M. blakemorei* and *M. gryphiswaldense* bacteria. The chain of magnetosomes can be clearly identified inside the bacteria. In the insets, a zoom-in of the chain is presented to showcase the different morphology of the magnetosomes from the two species.

temperatures), including the magnetocrystalline anisotropy contribution below T_v; and (iii) the Zeeman energy density term (E_Z). Considering θ and φ as the polar and azimuthal angles of the magnetic moment of each magnetosome, with the $\langle 100 \rangle$ magnetite crystallographic directions as reference, the total energy density is given by

$$E(\theta, \phi) = E_{cub}(\theta, \phi) + E_{uni}(\theta, \phi) + E_Z(\theta, \phi) \tag{1}$$

where

$$E_{\mathrm{cub}}(\theta, \phi) = \frac{K_{\mathrm{cub}}}{4}[\sin^4(\theta)\sin^2(2\phi) + \sin^2(2\theta)] \tag{2}$$

$$E_{\mathrm{uni}}(\theta, \phi) = K_{\mathrm{uni}}[1 - (\hat{u}_{\mathrm{m}} \cdot \hat{u}_{\mathrm{uni}})^2] \tag{3}$$

$$E_Z(\theta, \phi) = -\mu_0 M_S H(\hat{u}_{\mathrm{m}} \cdot \hat{u}_{\mathrm{H}}) \tag{4}$$

where K_{cub} is the effective cubic anisotropy constant, K_{uni} is the effective uniaxial anisotropy constant; $\hat{u}_{\mathrm{m}}$ is the magnetic moment unit vector; $\hat{u}_{\mathrm{uni}}$ is the unit vector along the effective uniaxial easy axis; $\hat{u}_{\mathrm{H}}$ is the external magnetic field unit vector; and M_s is the spontaneous magnetization of magnetite, $M_s = 48 \times 10^4$ A/m. The magnetosomes from *M. gryphiswaldense* present a quasi-uniaxial easy axis, $\hat{u}_{\mathrm{uni}}$, which is tilted ~20° out of the [111] chain axis, due to a slight deformation of their cuboctahedral shape.[26] However, for the magnetosomes from *M. blakemorei*, $\hat{u}_{\mathrm{uni}}$ is clearly pointing along the [111] chain axis due to its elongated shape. Taking into account these considerations, the M vs $\mu_0 H$ loops at different angles have been simulated, using a dynamic approach described by Carrey et al.,[49] and averaged in order to reproduce the experimentally obtained ZFC M vs $\mu_0 H$ loops corresponding to randomly oriented MTB. In this way, for each loop at a certain temperature, K_{cub} and K_{uni} have been adjusted to attain the best match between experimental and simulated M vs $\mu_0 H$ loops.

3. RESULTS AND DISCUSSION

To showcase the difference in the size and morphology of the magnetosomes of both species, we have carried out TEM analysis on the whole bacteria. Figure 1 shows representative TEM images of the *M. blakemorei* and *M. gryphiswaldense* bacteria and their chain of magnetosomes. As depicted, both species synthesize a single chain of magnetosomes, but in the case of *M. blakemorei*, these magnetosomes present an elongated truncated hexa-octahedral shape (see the inset to Figure 1), which differs from the cuboctahedral shape typically obtained for *M. gryphiswaldense* and other species of the genus *Magnetospirillum*. In both cases, the magnetosomes inside the chain are aligned along a [111] crystallographic direction of magnetite, which defines the so-called *chain axis*.[24] Concerning the chain of magnetosomes, it is noticeable that the length of the chain is larger in the case of *M. gryphiswaldense* with an average of ~15 magnetosomes per chain, while in the case of *M. blakemorei*, the average number of magnetosomes reduces to ~9 magnetosomes per chain. On the other hand, the dimensions of the magnetosomes from *M. blakemorei*, as determined from the corresponding TEM images, are 45(4) × 45(4) × 65(5) nm^3, while the cuboctahedral magnetosomes from *M. gryphiswaldense* have an average size of 45(5) nm. Despite the differences in their morphology, both magnetosomes present dimensions within a similar size range.

The different morphology of both strains results, naturally, in different shape anisotropy contributions. The shape anisotropy energy landscape has been calculated using a finite element method (FEM) protocol described in detail before (see refs 26,27), and the main results are summarized in Figure 2. This figure presents a schematic depiction of the morphology of each magnetosome, with the corresponding crystallographic axes and shape anisotropy energy landscape. In ref 26, by using FEM, we showed that the magnetosomes synthesized by *M. gryphiswaldense* present a slight deformation that gives rise to a deformed toroidal energy landscape, with a unique quasi-uniaxial character (i.e., a main uniaxial contribution + a smaller cubic contribution). This quasi-uniaxial easy axis is effectively tilted ~20° out of the [111] chain axis, as represented in Figure 2, and the corresponding shape anisotropy constant values are $K_{\mathrm{sh-uni}} \sim 7$ kJ m^{-3} and $K_{\mathrm{sh-cub}} \sim 1.5$ kJ m^{-3} at 300 K. Instead, in the case of *M. blakemorei*,[27] the shape anisotropy energy landscape exhibits a perfect toroidal shape, indicating the presence of a well-defined uniaxial easy axis along the chain axis direction. These magnetosomes exhibit some dispersion in their aspect ratio, i.e., width/length (W/L), with an average value: W/L = 0.70(6), which gives rise to a uniaxial shape anisotropy

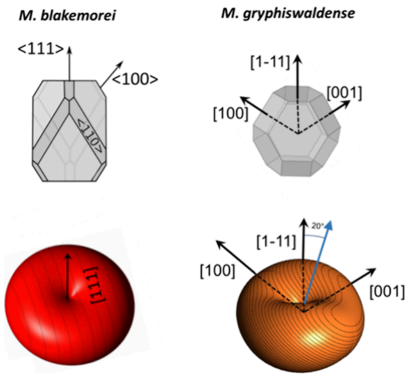

Figure 2. (Top) Schematic depiction of the morphology of the magnetosomes of *M. blakemorei* (left) and *M. gryphiswaldense* (right), including the crystallographic axes. The [111] direction corresponds with the chain axis of the MTB. (Bottom) Corresponding shape anisotropy energy landscapes, which have been calculated following the procedure described in Gandia et al.[26] Adapted from ref 26 with permission from the Royal Society of Chemistry.

constant value of $K_{\mathrm{sh-uni}} \sim 23(4)$ kJ m^{-3} at 300 K. This difference in shape anisotropy can be particularly important for their potential biomedical applications, as we have recently demonstrated in the context of magnetic hyperthermia.[50] Therefore, these results clearly display that the elongated morphology of *M. blakemorei* magnetosomes gives rise to a stronger and strictly uniaxial shape anisotropy compared to *M. gryphiswaldense*. This is going to have an important impact on their magnetic response, as we will see below.

To probe the influence of the different anisotropy energy landscapes on the magnetic properties, static magnetic measurements have been carried out, both as a function of the temperature (M vs T) and as a function of the magnetic field (M vs $\mu_0 H$), from 5 to 300 K. Figure 3a showcases the M vs T curves measured in the ZFC/FC mode at low fields, 5 mT, for both species. These ZFC/FC curves present a qualitatively similar behavior in both cases: there is a strong irreversibility between the ZFC and FC curves, and a sharp transition appears in both curves around 100−110 K, which corresponds to the well-known Verwey transition of magnetite.[51−53] As has been explained before, this is a temperature phase transition in which magnetite changes from cubic metallic inverse spinel structure to monoclinic insulator with decreasing temperature. This transition involves a shift in the easy axis of magnetization and a change in the magnetocrystalline anisotropy constant (K_1), as well as an increase in coercivity and anisotropy in the monoclinic phase.[53−55] The presence of the Verwey transition in the ZFC/FC curves is a clear indicator of the magnetosomes being made of $\mathrm{Fe_3O_4}$. In bulk magnetite, this transition gives rise to a sharp M(T) step around T_{v} = 120 K.[56,57] However, in magnetosomes, and in other high-quality magnetite nanoparticles, this transition tends to be slightly shifted and smoothed. This can be in principle related to the stoichiometry moving away from that of pure magnetite due to the presence of vacancies, defects, or doping elements.[58−62] In our case, the Verwey temperature is shifted ∼10 K toward lower temperatures for both species. This can be more easily discerned if we inspect the first derivative of the ZFC curves (Figure 3b), where a well-defined peak appears around 90−100 K, corresponding to the Verwey transition. This peak is slightly sharper for *M. blakemorei*, suggesting a more homogeneous stoichiometry. This is also supported by the value of the onset of the Verwey temperature (marked with black arrows): $T_{\mathrm{v}} \sim 112$ K for *M. blakemorei*, slightly closer to the expected bulk value, $T_{\mathrm{v}} \sim 120$ K, than for *M. gryphiswaldense*, $T_{\mathrm{v}} \sim 107$ K. In addition, as marked by the change in the slope of the ZFC curves and the second peak in the derivative, a second transition appears around 30−50 K. These correspond to the so-called "low-T transitions", frequently reported in bulk magnetite and magnetite-based nanoparticles, although their nature is still under debate.[63−68] As depicted in the derivative, there are some small differences in the shape and position (marked by white arrows) of this low T peak, around $T_{\mathrm{low\text{-}T}} \sim 27$ and ∼30 K for *M. blakemorei* and *M. gryphiswaldense*, respectively. Therefore, these results indicate similar crystallographic transitions in both magnetosomes despite their marked difference in morphology.

Next, in order to gain a better insight into the complex interplay of anisotropies in these two MTB species, their magnetic response as a function of the applied magnetic field has been analyzed by measuring the M vs $\mu_0 H$ loops up to 1 T

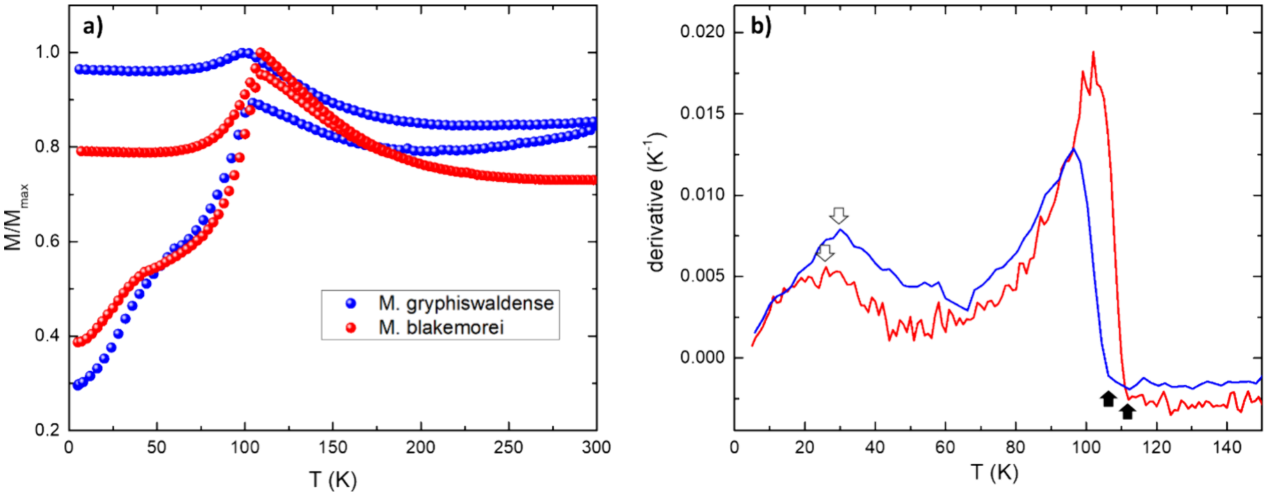

Figure 3. (a) ZFC/FC curves measured at 5 mT for *M. blakemorei* and *M. gryphiswaldense*. (b) First derivative of the ZFC curve (5−150 K). Arrows in the plot mark the two transitions discussed in text, i.e., low-T transition (white arrows) and the onset of the Verwey transition (black arrows).

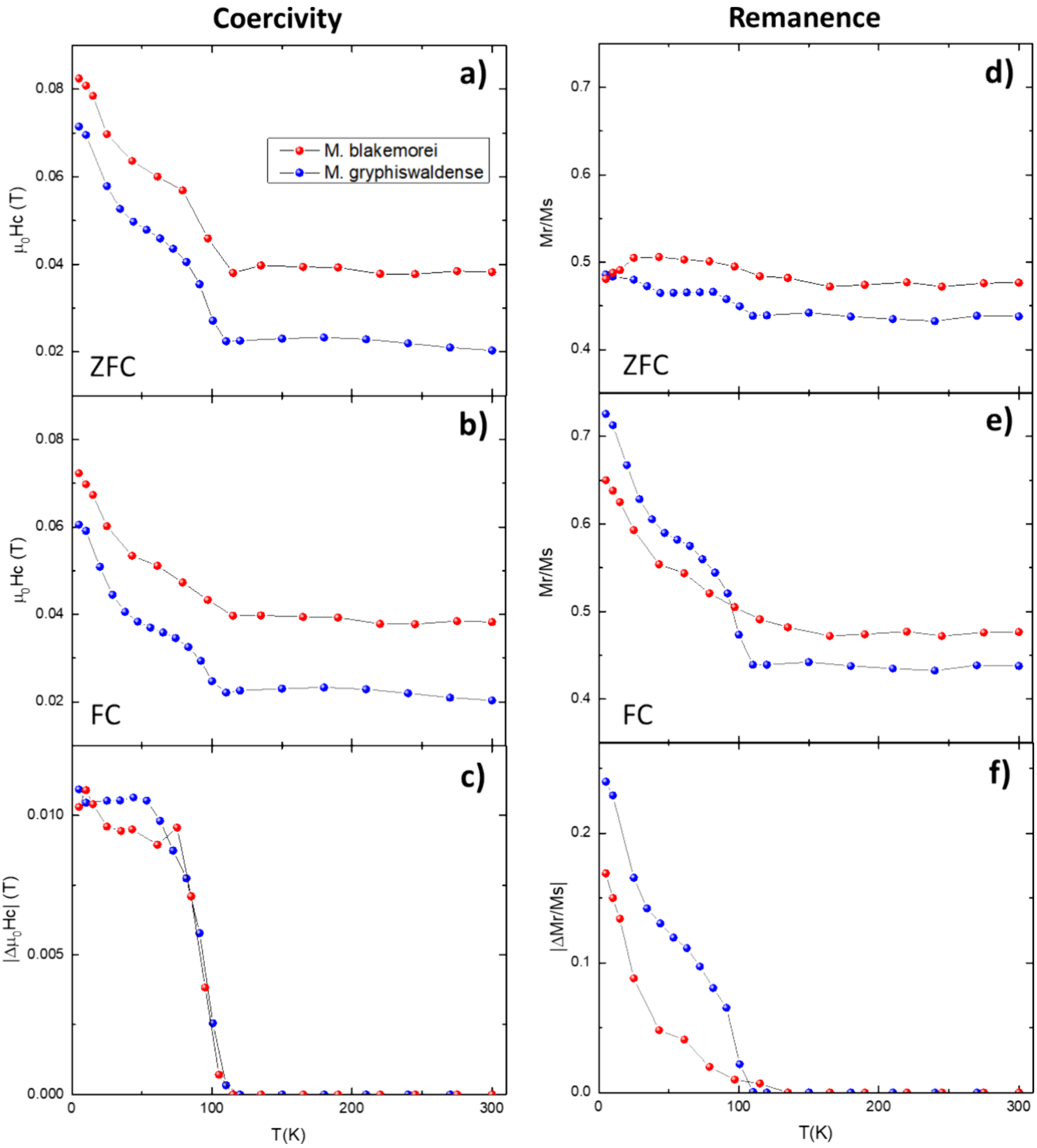

Figure 4. Thermal evolution of the (a) ZFC and (b) FC coercive field, μ_0H_c, (d) ZFC and (e) FC normalized remanence, M_r/M_s, vs temperature curves obtained from the corresponding M vs μ_0H loops. The difference, in absolute value, between these FC and ZFC curves is represented in (c) for the coercive field, $|\Delta\mu_0H_c|$, and in (f) for the normalized remanence, $|\Delta M_r/M_s|$.

at different temperatures between 5 and 300 K, in both ZFC and FC modes for *M. blakemorei* (see Figure S1 in the Supporting Information). Briefly, above T_v, the ZFC and FC hysteresis loops are nearly identical, but as the temperature decreases, the FC loops show lower coercivity and higher remanence than the ZFC loops; additionally, *M. blakemorei* exhibits wider loops with higher irreversibility than *M. gryphiswaldense*, indicative of higher effective anisotropy. To better analyze the differences, in Figure 4, we have represented the thermal evolution of the coercive field, μ_0H_c (left), and the normalized magnetization remanence, M_r/M_s (right), for both species.

The evolution of μ_0H_c with temperature (Figures 4a,b) is qualitatively similar for both bacteria species, but the obtained values are appreciably higher (up to two times greater) for *M. blakemorei*. This enhanced coercivity can be directly associated with the higher shape anisotropy of *M. blakemorei*, since it is proportional to the anisotropy: $H_c = 2K/\mu_0M_s$ for single domain uniaxial nanoparticles, following a *coherent rotation* or *Stoner–Wohlfarth* mode during the reversal of the magnet-

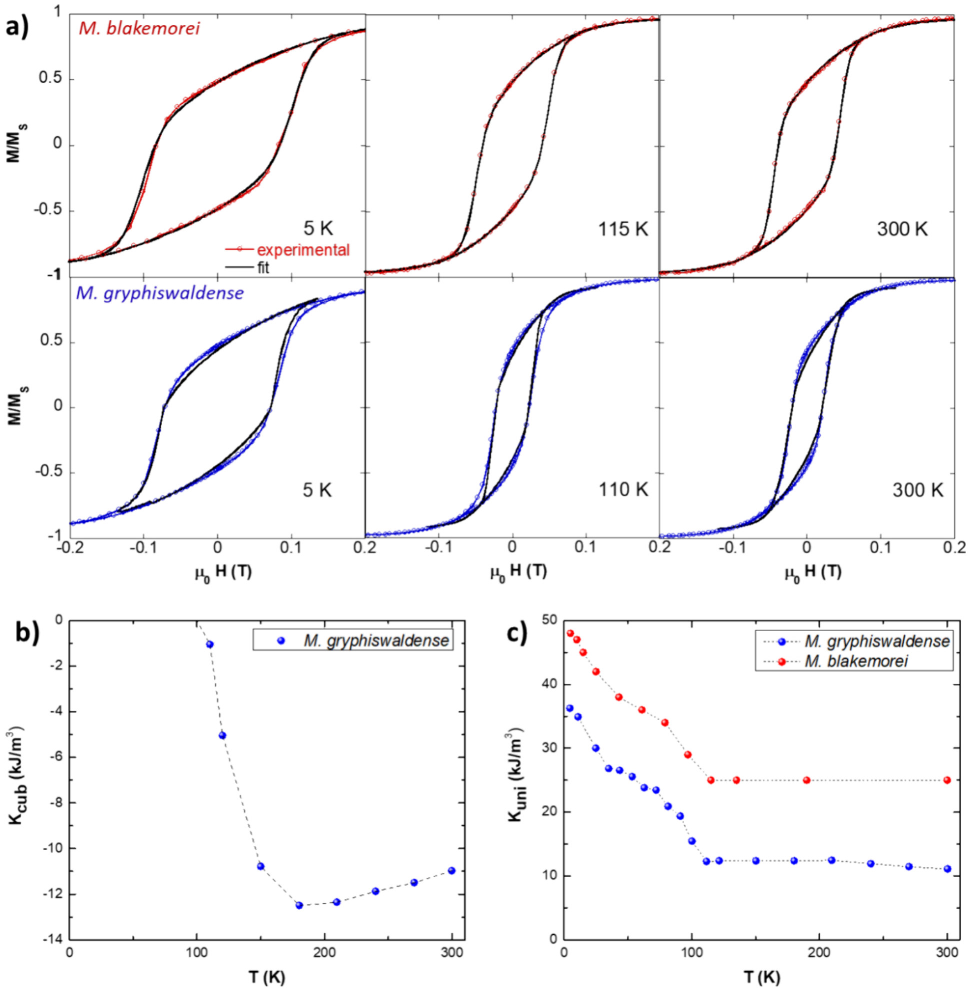

Figure 5. (a) Experimental and simulated ZFC M vs μ_0H loops at 5, 115, and 300 K obtained for *M. blakemorei* and *M. gryphiswaldense*. Thermal evolution of the effective (b) cubic anisotropy (K_{cub}) and (c) uniaxial anisotropy (K_{uni}) as obtained from the simulations.

ization.[69] This shows that changing the shape of MNPs is a powerful strategy to tune the coercive field, which is especially interesting in different applications such as magnetic hyperthermia or data storage.[30,32,70,71] Concerning the thermal evolution, we can see that $\mu_0H_{c\text{-ZFC}}$ remains nearly constant ($\mu_0H_{c\text{-ZFC}}$ = 40 and 20 mT for *M. blakemorei* and *M. gryphiswaldense*, respectively) from 300 K down to ∼110 K, that is, T_v. In the case of bulk magnetite, the coercive field steeply increases below T_v, and then remains nearly constant,[72] which is related to the sharp transition taking place: with decreasing temperature, the magnetocrystalline anisotropy changes from cubic (⟨111⟩ easy axes) to essentially uniaxial (⟨100⟩ easy axes) as the crystalline structure evolves from cubic to monoclinic, giving rise to a sudden increase in the coercive field.[73,74] However, in the case of magnetosomes and many other magnetite-based nanoparticles,[58,75,76] this process is, unsurprisingly, less abrupt and more complex than in bulk. Here, we can see that $\mu_0H_{c\text{-ZFC}}$ first increases below T_v, following which there is a shoulder around 70−75 K, and finally increases again below 40−45 K, reaching a maximum value at 5 K of 80 and 70 mT for *M. blakemorei* and *M. gryphiswaldense*, respectively. A similar behavior, albeit smoother, is obtained for the $\mu_0H_{c\text{-FC}}$ curves (Figure 4b). The differences between both MTB can be better tracked by representing the relative change of the coercive field, $|\Delta\mu_0H_c|$ vs T curves (Figure 4c). As depicted, the curves nearly overlap for both samples, indicating that, despite the difference in coercive field values, the magnetic response and the magnetic transitions taking place are very similar. However, there are minor differences below 70 K, which indicate some changes in the magnetocrystalline anisotropy of both samples, as had already been showcased in the M vs T curves.

Focusing now on the normalized remanence, on the one hand, it can be observed that the ZFC $M_r/M_{S\text{-ZFC}}$ (Figure 4d) remains fairly constant for both MTB species: for *M. gryphiswaldense*, $M_r/M_{S\text{-ZFC}}$ ∼ 0.44 from 300 K down to 110 K, and then it increases up to $M_r/M_{S\text{-ZFC}}$ ∼ 0.49 at 5 K; for *M. blakemorei*, $M_r/M_{S\text{-ZFC}}$ ∼ 0.48 from 300 K down to 110 K, and then increases up to 0.50. These values are close to ∼0.5, indicating that, overall, these magnetosomes behave like randomly oriented uniaxial single domain magnetic nanoparticles, as typically described in the framework of the Stoner−Wohlfarth model.[77] This behavior is more closely followed by the elongated magnetosomes from *M. blakemorei*, as expected, due to their better-defined uniaxial shape anisotropy. On the other hand, in the case of the FC remanence values, $M_r/M_{S\text{-FC}}$ (Figure 4e), we can see, however, some clear changes. For *M. gryphiswaldense*, $M_r/M_{S\text{-FC}}$ increases abruptly from 0.44 below the Verwey transition up to 0.72 at 5 K. Noticeably, a shoulder around 60 K, resembling the one observed in the μ_0H_c vs T curves, is also present in these $M_r/M_{S\text{-FC}}$ vs T curves. On the other hand, for *M.*

blakemorei, we see a more progressive evolution: $M_r/M_{S\text{-FC}}$ remains nearly constant, ∼0.48, from 300 to 160 K, and then it increases up to 0.65 at 5 K. The relative change of the normalized remanence, $|\Delta M_r/M_S|$ vs T (Figure 4f), allows to better detect the differences between both MTB. Above T_v, $|\Delta M_r/M_S|$ is null for both species, but below T_v, a progressive increase in $|\Delta M_r/M_S|$ is obtained, more abrupt in the case of *M. gryphiswaldense*.

Therefore, these results indicate that, despite the similarities between both MTB, there are some clear differences in their magnetic response, which can be related to the various anisotropies influencing the magnetic behavior of these bacteria. To fully capture the physics underneath, computational simulations of the experimental M vs $\mu_0 H$ loops have been carried out, as described in Section 2. The experimental and simulated ZFC M vs $\mu_0 H$ loops obtained at 5, 115, and 300 K for *M. blakemorei* and *M. gryphiswaldense* using this model have been represented in Figure 5a. As depicted, an excellent match between experimental values and simulations has been reached in all cases by properly tuning the values of K_{cub} and K_{uni}. Similar results have been obtained for the rest of the temperatures. These have allowed us to plot the thermal evolution of both anisotropy constants, as depicted in Figure 5b,c. Interestingly, while in the case of *M. gryphiswaldense* both K_{cub} and K_{uni} need to be included in the model in order to obtain a good fitting above T_v, in the case of *M. blakemorei*, only K_{uni} needs to be taken into consideration in the whole temperature range. For the latter, the strong uniaxial anisotropy energy, E_{uni}, in the [111] direction makes the cubic magnetocrystalline anisotropy energy, E_{cub}, irrelevant for these calculations, and the shape of the calculated M vs $\mu_0 H$ loops does not change by including the E_{cub} term. Therefore, we have not considered this term for *M. blakemorei*, and only the effective uniaxial anisotropy term, E_{uni}, has been included in the simulations of this species, with a Gaussian distribution to take into account the aspect ratio dispersion existing in these specific magnetosomes (i.e., W/L = 0.70(6)). This explains why K_{cub} is only represented for *M. gryphiswaldense* in Figure 5b.

The thermal evolution of the cubic contribution to anisotropy, K_{cub}, is mainly related to magnetocrystalline anisotropy. Although it is true that magnetosomes from *M. gryphiswaldense* present a non-negligible cubic contribution to the shape anisotropy, $K_{sh-cub} = 1.5$ kJ m^{-3} at 300 K,[26] this value is nearly one order of magnitude smaller than the magnetocrystalline contribution. In Figure 5b, it can be observed that at room temperature, the obtained value of K_{cub} is around −11.0 kJ m^{-3}, close to the expected K_{cub} value for bulk magnetite, −10.8 kJ m^{-3}. With decreasing temperature, K_{cub} slowly increases in absolute value up to −12.5 kJ m^{-3} at 180 K. After that, it rapidly decreases in absolute value until becoming null at 110 K, around the Verwey transition. The thermal evolution of K_{cub} above the Verwey transition is very similar to what has been reported in the literature for bulk magnetite (see for example Abe et al.[73] or Bickford et al.[78]). This serves as a reminder of the well-known high structural quality of these magnetosomes.

Concerning the thermal evolution of the uniaxial contribution, K_{uni}, it is important to recall that, above the Verwey temperature, it gathers two contributions: the shape uniaxial anisotropy ($K_{sh\text{-}uni}$) and the dipolar interactions between magnetosomes inside the chain (K_{dip}). On the other hand, below the Verwey temperature, a third contribution should appear, associated with magnetocrystalline anisotropy. In Figure 5b, already at 300 K, we can see some clear differences between the two species analyzed in this work: the K_{uni} value for *M. blakemorei* (∼25 kJ m^{-3}) is appreciably higher than the one obtained for *M. gryphiswaldense* (∼11 kJ m^{-3}). Since the values for the shape anisotropy of both magnetosomes at 300 K have already been calculated using our FEM model[26] (∼7 kJ m^{-3} for *M. gryphiswaldense* and ∼23 kJ m^{-3} for *M. blakemorei*), we can directly obtain an estimation of the effective dipolar anisotropy. Although, contrary to other models, such as Landau−Lifshitz−Gilbert,[26,79,80] magnetostatic interactions are not explicitly calculated in this dynamic Stoner−Wohlfarth model, due to the alignment of the magnetosomes within the chain, their contribution can be directly estimated as $K_{dip} = K_{uni} - K_{sh\text{-}uni}$, being $K_{dip} \sim 4$ kJ m^{-3} for *M. gryphiswaldense* and ∼2 kJ m^{-3} for *M. blakemorei*. The difference in K_{dip} values between the two bacteria could be related to the fact that, as observed in the TEM analysis, *M. gryphiswaldense* presents on average longer chains than *M. blakemorei*.

From 300 to 110 K, i.e., down to the Verwey transition, K_{uni} remains almost constant for both species (there is a slight increase in the case of *M. gryphiswaldense*). This indicates that the thermal dependence of both shape and dipolar anisotropies, in this range of temperatures, is relatively small. However, below the Verwey temperature, K_{uni} increases from 12 to 36 kJ m^{-3} at 5 K for *M. gryphiswaldense*, and from 25 to 48 kJ m^{-3} at 5 K in the case of *M. blakemorei*. The evolution of K_{uni} vs T below the Verwey transition follows the same qualitative trend we saw for $\mu_0 H_c$ vs T: a first increase with a shoulder between 75 and 35 K, approximately, and a second increase below that temperature down to 5 K. This increase in K_{uni} is associated, as explained before, with the change in magnetocrystalline anisotropy, from cubic to uniaxial. Here, we must clarify that it is well known that the cubic-to-monoclinic transition during cooling through the Verwey transition results in a change from cubic anisotropy to essentially uniaxial anisotropy along the ⟨100⟩ crystallographic directions. However, our observations indicate that, in order to properly reproduce the experimental hysteresis loops of the magnetosomes at low temperature, we must assume an intrinsic preferential alignment of the three ⟨100⟩ crystallographic directions. Specifically, in the absence of an applied field, the orthorhombic deformation would preferentially occur along the ⟨100⟩ direction closest to the easy magnetization axis ($\hat{u}_{uni}$) of each magnetosome. This behavior is consistent with the shape and dipolar contributions present in these nanoparticles. When an external field is applied during the cooling process, the three ⟨100⟩ directions become equally probable, setting the easy magnetization axis along that ⟨100⟩ direction that is closer to the direction of the applied field.[81] Thus, in the FC measurements, two-thirds of the orthorhombic deformation will take place along the ⟨100⟩ direction closer to $\hat{u}_{uni}$, while one-third will occur along the remaining ⟨100⟩ direction, which is approximately perpendicular to $\hat{u}_{uni}$. This competition leads to a decrease in the effective uniaxial anisotropy in the FC case compared to the ZFC case, explaining, for example, the experimentally observed reduction in coercivity during FC measurements as observed in the experimental M vs $\mu_0 H$ loops (see Figure 4).

Concerning the shape and dipolar anisotropies, as it is well known, their thermal dependence should be proportional to thermal evolution of M_S^2.[69] Our results indicate that above the Verwey temperature, the saturation magnetization roughly

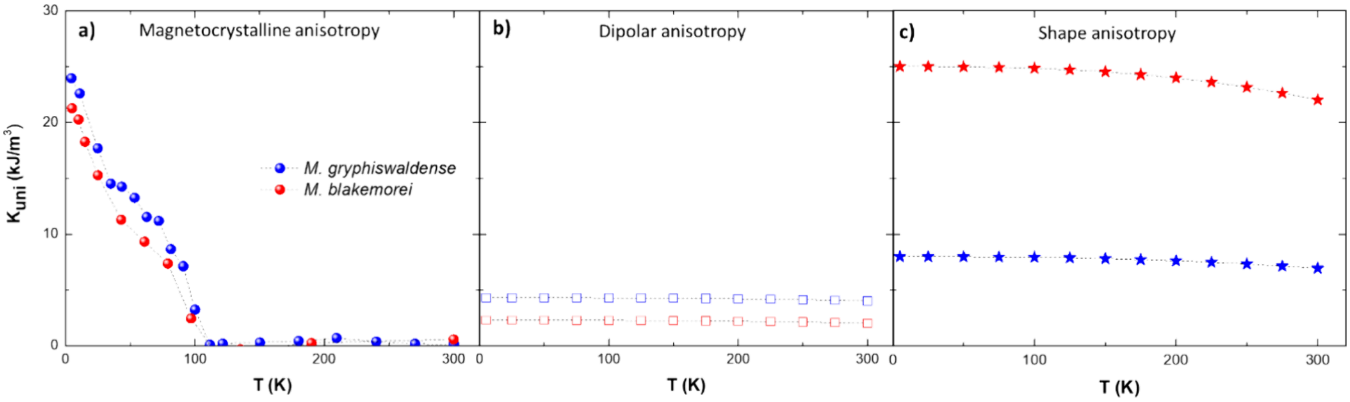

Figure 6. Thermal evolution of the (a) magnetocrystalline, (b) dipolar, and (c) shape anisotropies to the effective uniaxial anisotropy constant, K_{uni}, for *M. gryphiswaldense* and *M. blakemorei*.

follows a Bloch-like law, $M_s(T) \propto M_0[1 - (\frac{T}{T_0})^{\alpha_B}]$, with M_0 being the saturation magnetization at 0 K, T_0 the temperature at which M_s becomes null, i.e., the Curie temperature (~843 K for magnetite), and α_B is a Bloch-like exponent (see Figure S2). In our case, α_B acquires a value ~2.65. Note that the slight experimental drop in $M_s(T)$ below the Verwey transition obtained in Figure S2 has been previously described in bulk magnetite.[72] By using the values obtained from our calculations for K_{dip} and K_{sh-uni} at 300 K as starting points, and considering that the thermal evolution of both anisotropies should be proportional to $M_S^2(T)$, we have applied the same Bloch-like law for the shape and dipolar contributions, thereby obtaining the following expressions:

$$K_{dip}(T) = K_{dip0}\left[1 - \left(\frac{T}{T_0}\right)^{\alpha_B}\right]^2 \tag{5}$$

$$K_{sh-uni}(T) = K_{sh-uni0}\left[1 - \left(\frac{T}{T_0}\right)^{\alpha_B}\right]^2 \tag{6}$$

where K_{dip0} and $K_{sh-uni0}$ are the extrapolated dipolar and shape anisotropy constant values at 0 K, respectively.

This is more clearly illustrated in Figure 6, where the thermal evolution of the shape, dipolar, and magnetocrystalline contributions to the effective uniaxial anisotropy constant, K_{uni}, have been represented separately for both species. As depicted, for the shape and dipolar contributions, the change between 300 and 5 K is very small, <10%. By subtracting both shape and dipolar contributions from K_{uni}, we can obtain the uniaxial magnetocrystalline anisotropy contribution for each species. As depicted, the uniaxial magnetocrystalline anisotropy contributions for both MTB species follow a qualitatively similar evolution, much more complex than the shape and dipolar counterparts. Above T_v, the uniaxial magnetocrystalline contribution is null, as expected, but below T_v, it progressively increases with decreasing temperature following a non-monotonic trend. First, it rapidly increases up to ~8−10 kJ m^{-3} at 70 K, and then it describes a shoulder, reaching ~12−14 kJ m^{-3} at 40 K, and finally it increases again up to ~22−24 kJ m^{-3} at 5 K.

This behavior clearly differs from the one obtained in stoichiometric bulk magnetite, in which the transition from a cubic to a monoclinic structure is sharp. Therefore, these results indicate that in magnetosomes and other similar high-quality magnetite-based nanoparticles, instead of having an abrupt Verwey transition in a very narrow range of temperature, the transition is slower and more complex, as described before. Interestingly, this evolution of the uniaxial magnetocrystalline anisotropy resembles the one from the ZFC curves (see Figure S3), suggesting that the "low T transition" appearing around 30−50 K in these and other magnetite-based nanoparticles could be linked to the change in the uniaxial magnetocrystalline anisotropy evolution observed around the same range of temperatures. The reasons behind this complex behavior could be related to the presence of a distribution of defects, vacancies, and/or doping elements in the crystalline structure of these nanoparticles. It is well known that magnetite is greatly affected by tiny structural modifications.[68,82] These structural modifications could contribute to a progressive change in the crystalline structure, from cubic to monoclinic with decreasing temperature, although further experiments would be needed to shed more light on this matter.

It is important to emphasize that this distinction of individual contributions from experimental measurements represents a significant achievement, as such differentiation is often exceedingly difficult with other magnetite-based nanoparticles. This underscores the exceptional utility of magnetosomes as ideal model magnetic nanoparticles.

4. CONCLUSIONS

In this study, we successfully isolated and analyzed the diverse anisotropic contributions affecting the magnetic properties of magnetite-based nanoparticles. Using magnetosomes from two MTB species, *M. gryphiswaldense* and *M. blakemorei*, which display similar composition, dimensions, and crystallinity but very different shape (K_{sh} ~ 7 kJ/m^3 and ~23 kJ/m^3 at 300 K, respectively), we conducted a comparative analysis while maintaining consistency in other influential parameters. The dipolar interactions contributed a minor uniaxial anisotropy of approximately 2−4 kJ/m^3 at 300 K. Despite minimal thermal variations in both shape and dipolar anisotropies across the examined temperature range, the differences in shape anisotropy between both species markedly influenced the M vs H loops, notably enhancing the coercivity for *M. blakemorei* by up to twofold compared to *M. gryphiswaldense*. This underscores the critical role of shape anisotropy in modifying magnetic hysteresis in nanoparticles, which is especially relevant for applications of these nanoparticles in different fields, including biomedicine.

Furthermore, the uniaxial contribution of magnetocrystalline anisotropy was found to predominantly affect magnetic behavior at lower temperatures. Through computations using a dynamic Stoner–Wohlfarth model, we were able to distinctly separate and trace the thermal evolution of the various anisotropic contributions: shape, dipolar, and magnetocrystalline. Notably, the intricate magnetic behavior observed in magnetosomes and other magnetite-based nanoparticles below the Verwey transition ($T_v \sim 110-120$ K) is governed by a nonmonotonic increase in uniaxial magnetocrystalline anisotropy as temperature decreases. This triggers a progressive Verwey transition, with the magnetite structure transitioning from cubic to monoclinic, where the uniaxial magnetocrystalline anisotropy contribution reaches a final value around 22–24 kJ/m^3 at 5 K. Despite the similar behavior in both species, our method has allowed us to pinpoint small differences in the magnetocrystalline anisotropy of their magnetosomes.

These findings highlight the exceptional utility of magnetosomes as ideal model nanoparticles for detailed studies, where a combination of experimental measurements and computational simulations facilitates a comprehensive understanding of the different factors influencing the magnetic responses of nanoparticles. This work not only enhances our understanding of magnetic nanoparticle behavior but also demonstrates the potential applications of magnetosomes in nanomagnetic research.

■ ASSOCIATED CONTENT

Supporting Information

The Supporting Information is available free of charge at https://pubs.acs.org/doi/10.1021/acsomega.4c09371.

> M–H loops measured in ZFC and FC modes at different temperatures; *Ms* vs *T* evolution and the corresponding Bloch law fitting; and comparison between the thermal evolution of the ZFC magnetization and the uniaxial magnetocrystalline anisotropy of *M. gryphiswaldense*(PDF)

■ AUTHOR INFORMATION

Corresponding Authors

Mª Luisa Fdez-Gubieda – *Departamento de Electricidad y Electrónica, Universidad del País Vasco (UPV/EHU), Leioa 48940, Spain;* orcid.org/0000-0001-6076-7738; Phone: +34 94 601 2552; Email: malu.gubieda@ehu.eus

Javier Alonso – *Departamento de CITIMAC, Universidad de Cantabria, Santander 39005, Spain;* orcid.org/0000-0003-0045-5390; Phone: +34 94 220 1621; Email: javier.alonsomasa@unican.es

Authors

David Gandia – *Departamento de Ciencias, Universidad Pública de Navarra, Pamplona 31006, Spain;* orcid.org/0000-0003-2203-6752

Lourdes Marcano – *Departamento de Física, Universidad de Oviedo, Oviedo 33007, Spain; CIC biomaGUNE, Basque Research and Technology Alliance (BRTA), Donostia-San Sebastián 20014, Spain*

Lucía Gandarias – *Departamento de Inmunología, Microbiología y Parasitología, Universidad del País Vasco (UPV/EHU), Leioa 48940, Spain; Aix-Marseille Institute of Biosciences and Biotechnologies (BIAM), Aix-Marseille Université, CNRS, CEA – UMR 7265, Saint-Paul-lez-Durance 13108, France;* orcid.org/0000-0001-5749-971X

Alicia G. Gubieda – *Departamento de Inmunología, Microbiología y Parasitología, Universidad del País Vasco (UPV/EHU), Leioa 48940, Spain;* orcid.org/0000-0002-7598-2008

Ana García-Prieto – *Departamento de Física Aplicada, Universidad del País Vasco (UPV/EHU), Bilbao 48013, Spain*

Luis Fernández Barquín – *Departamento de CITIMAC, Universidad de Cantabria, Santander 39005, Spain*

Jose Ignacio Espeso – *Departamento de CITIMAC, Universidad de Cantabria, Santander 39005, Spain;* orcid.org/0000-0002-4018-7186

Elizabeth Martín Jefremovas – *Institute of Physics, Johannes Gutenberg University of Mainz, Mainz 55128, Germany; Department of Physics and Materials Science, University of Luxembourg, Luxembourg L-1511, Grand Duchy of Luxembourg; Institute for Advanced Studies, University of Luxembourg, Esch-sur-Alzette L-4365, Luxembourg;* orcid.org/0000-0001-8501-058X

Iñaki Orue – *SGIker, Universidad del País Vasco (UPV/EHU), Leioa 48940, Spain;* orcid.org/0000-0002-7496-2566

Ana Abad Diaz de Cerio – *Departamento de Inmunología, Microbiología y Parasitología, Universidad del País Vasco (UPV/EHU), Leioa 48940, Spain;* orcid.org/0000-0001-6022-1751

Complete contact information is available at: https://pubs.acs.org/10.1021/acsomega.4c09371

Author Contributions

David Gandia: investigation, methodology, formal analysis, visualization, and writing—review and editing. Lourdes Marcano: investigation, formal analysis, visualization, and writing—review and editing. Lucía Gandarias: investigation, methodology, formal analysis, visualization, and writing—review and editing. Alicia G. Gubieda: investigation and writing—review and editing. Ana García Prieto: conceptualization, project administration, funding acquisition, and writing—review and editing. Luis Fernández Barquín: project administration, funding acquisition, resources, supervision, and writing—review and editing. José Ignacio Espeso: investigation and data curation. Elizabeth Martín Jefremovas: investigation and writing—review and editing. Iñaki Orue: resources, validation, methodology, and investigation. Ana Abad Díaz de Cerio: resources, validation, conceptualization, and supervision. Mª Luisa Fdez-Gubieda: conceptualization, project administration, funding acquisition, resources, validation, supervision, and writing—review and editing. Javier Alonso: conceptualization, project administration, funding acquisition, formal analysis, writing—original draft, visualization, and writing—review and editing.

Notes

The authors declare no competing financial interest.

This article does not contain any studies with human participants or animals performed by any of the authors.

■ ACKNOWLEDGMENTS

This work has been funded by the Spanish Government (grants PID2020-115704RB-C3 and PID2023-146448OB-C2 funded by MICIU/AEI/10.13039/501100011033/FEDER, UE) and the Basque Government (grant IT1479-22). L.G. would like to acknowledge the financial support provided through a postdoctoral fellowship from the Basque Government (POS_2022_1_0017). L.M. thanks the Horizon Europe Programme for the financial support provided through a Marie Sklodowska-Curie fellowship (101067742) and the BBVA Foundation for the Leonardo Fellowships for Researchers and Cultural Creators 2022. E.M.J. has received funding from the European Union's Horizon 2020 research and innovation programme under the Marie Skłodowska-Curie Actions grant agreement 101081455 - YIA and from the Institute for Advanced Studies (IAS) of the University of Luxembourg for a postdoctoral fellowship. The authors thank SGIker (UPV/EHU/ERDF, EU) for technical and human support.

■ REFERENCES

(1) Bazylinski, D. A.; Williams, T. J.; Lefèvre, C. T.; Trubitsyn, D.; Fang, J.; Beveridge, T. J.; Moskowitz, B. M.; Ward, B.; Schübbe, S.; Dubbels, B. L.; Simpson, B. Magnetovibrio blakemorei Gen. Nov., Sp. Nov., a Magnetotactic Bacterium (Alphaproteobacteria: Rhodospirillaceae) Isolated from a Salt Marsh. *Int. J. Syst. Evol Microbiol* **2013**, *63*, 1824−1833.

(2) Bazylinski, D. A.; Frankel, R. B. magnetosome Formation in Prokaryotes. *Nat. Rev. Microbiol* **2004**, *2*, 217−230.

(3) Blakemore, R. P. Magnetotactic Bacteria. *Annu. Rev. Microbiol.* **1982**, *36*, 217−238.

(4) Komeili, A.; Vali, H.; Beveridge, T. J.; Newman, D. K. magnetosome Vesicles Are Present before Magnetite Formation, and MamA Is Required for Their Activation. *Proc. Natl. Acad. Sci. U. S. A.* **2004**, *101*, 3839−3844.

(5) Frankel, R. B.; Dunin-Borkowski, R. E.; Pósfai, M.; Bazylinski, D. A. Magnetic Microstructure of Magnetotactic Bacteria. *In Handbook of Biomineralization: Biological Aspects and Structure Formation* **2007**, *1*, 126−144.

(6) Gandia, D.; Gandarias, L.; Rodrigo, I.; Robles-García, J.; Das, R.; Garaio, E.; García, J. Á.; Phan, M. H.; Srikanth, H.; Orue, I.; Alonso, J.; Muela, A.; Fdez-Gubieda, M. L. Unlocking the Potential of Magnetotactic Bacteria as Magnetic Hyperthermia Agents. *Small* **2019**, *15*, No. 1902626.

(7) Fdez-Gubieda, M. L.; Alonso, J.; García-Prieto, A.; García-Arribas, A.; Fernández Barquín, L.; Muela, A. Magnetotactic Bacteria for Cancer Therapy. *J. Appl. Phys.* **2020**, *128*, No. 070902.

(8) Alphandéry, E. Applications of Magnetosomes Synthesized by Magnetotactic Bacteria in Medicine. *Front. Bioeng. Biotechnol.* **2014**, *2*, 5.

(9) Mokrani, N.; Felfoul, O.; Zarreh, F. A.; Mohammadi, M.; Aloyz, R.; Batist, G.; Martel, S. Magnetotactic Bacteria Penetration into Multicellular Tumor Spheroids for Targeted Therapy. *Annu. Int. Conf. IEEE Eng. Med. Biol. Soc.* **2010**, 4371−4374.

(10) Xiang, Z.; Yang, X.; Xu, J.; Lai, W.; Wang, Z.; Hu, Z.; Tian, J.; Geng, L.; Fang, Q. Tumor Detection Using magnetosome Nanoparticles Functionalized with a Newly Screened EGFR/HER2 Targeting Peptide. *Biomaterials* **2017**, *115*, 53−64.

(11) Martel, S.; Mohammadi, M.; Felfoul, O.; Zhao, Lu; Pouponneau, P. Flagellated Magnetotactic Bacteria as Controlled MRI-Trackable Propulsion and Steering Systems for Medical Nanorobots Operating in the Human Microvasculature. *Int. J. Rob. Res.* **2009**, *28*, 571−582.

(12) Mathuriya, A. S. Magnetotactic Bacteria for Cancer Therapy. *Biotechnol. Lett.* **2015**, *37*, 491−498.

(13) Vargas, G.; Cypriano, J.; Correa, T.; Leão, P.; Bazylinski, D.; Abreu, F. Applications of Magnetotactic Bacteria, Magnetosomes and magnetosome Crystals in Biotechnology and Nanotechnology: Mini-Review. *Molecules* **2018**, *23*, 2438.

(14) Muela, A.; Muñoz, D.; Martín-Rodríguez, R.; Orue, I.; Garaio, E.; Abad Díaz de Cerio, A.; Alonso, J.; García, J. Á.; Fdez-Gubieda, M. L. Optimal Parameters for Hyperthermia Treatment Using Biomineralized Magnetite Nanoparticles: Theoretical and Experimental Approach. *J. Phys. Chem. C* **2016**, *120*, 24437−24448.

(15) Mirkhani, N.; Christiansen, M. G.; Gwisai, T.; Menghini, S.; Schuerle, S. Spatially Selective Delivery of Living Magnetic Microrobots through Torque-Focusing. *Nat. Commun.* **2024**, *15*, 1−14.

(16) Jefremovas, E. M.; Gandarias, L.; Rodrigo, I.; Marcano, L.; Gruttner, C.; Garcia, J. A.; Garayo, E.; Orue, I.; Garcia-Prieto, A.; Muela, A.; Fernandez-Gubieda, M. L.; Alonso, J.; Barquin, L. F. Nanoflowers versus Magnetosomes: Comparison between Two Promising Candidates for Magnetic Hyperthermia Therapy. *IEEE Access* **2021**, *9*, 99552−99561.

(17) Gandarias, L.; Jefremovas, E. M.; Gandia, D.; Marcano, L.; Martínez-Martínez, V.; Ramos-Cabrer, P.; Chevrier, D. M.; Valencia, S.; Fernández Barquín, L.; Fdez-Gubieda, M. L.; Alonso, J.; García-Prieto, A.; Muela, A. Incorporation of Tb and Gd Improves the Diagnostic Functionality of Magnetotactic Bacteria. *Mater. Today Bio* **2023**, *20*, No. 100680.

(18) Amor, M.; Wan, J.; Egli, R.; Carlut, J.; Gatel, C.; Andersen, I. M.; Snoeck, E.; Komeili, A. Key Signatures of Magnetofossils Elucidated by Mutant Magnetotactic Bacteria and Micromagnetic Calculations. *J. Geophys Res. Solid Earth* **2022**, *127*, No. e2021JB023239.

(19) Marmol, M.; Gachon, E.; Faivre, D. Colloquium: Magnetotactic Bacteria: From Flagellar Motor to Collective Effects. *Rev. Mod. Phys.* **2024**, *96*, 21001.

(20) Rupprecht, J. F.; Waisbord, N.; Ybert, C.; Cottin-Bizonne, C.; Bocquet, L. Velocity Condensation for Magnetotactic Bacteria. *Phys. Rev. Lett.* **2016**, *116*, No. 168101.

(21) Petroff, A.; Rosselli-Calderon, A.; Roque, B.; Kumar, P. Phases of Active Matter Composed of Multicellular Magnetotactic Bacteria near a Hard Surface. *Phys. Rev. Fluids* **2022**, *7*, 53102.

(22) Gwisai, T.; Mirkhani, N.; Christiansen, M. G.; Nguyen, T. T.; Ling, V.; Schuerle, S. Magnetic Torque-Driven Living Microrobots for Increased Tumor Infiltration. *Sci. Robot* **2022**, *7*, No. eabo0665.

(23) Goswami, P.; He, K.; Li, J.; Pan, Y.; Roberts, A. P.; Lin, W. Magnetotactic Bacteria and Magnetofossils: Ecology, Evolution and Environmental Implications. *NPJ. Biofilms Microbiomes* **2022**, *8*, 1−14.

(24) Orue, I.; Marcano, L.; Bender, P.; García-Prieto, A.; Valencia, S.; Mawass, M. A.; Gil-Cartón, D.; Alba Venero, D.; Honecker, D.; García-Arribas, A.; Fernández Barquín, L.; Muela, A.; Fdez-Gubieda, M. L. Configuration of the magnetosome Chain: A Natural Magnetic Nanoarchitecture. *Nanoscale* **2018**, *10*, 7407−7419.

(25) Jefremovas, E. M.; Gandarias, L.; Marcano, L.; Gacía-Prieto, A.; Orue, I.; Muela, A.; Fdez-Gubieda, M. L.; Barquín, L. F.; Alonso, J. Modifying the Magnetic Response of Magnetotactic Bacteria: Incorporation of Gd and Tb Ions into the magnetosome Structure. *Nanoscale Adv.* **2022**, *4*, 2649−2659.

(26) Gandia, D.; Gandarias, L.; Marcano, L.; Orue, I.; Gil-Cartón, D.; Alonso, J.; García-Arribas, A.; Muela, A.; Fdez-Gubieda, M. L. Elucidating the Role of Shape Anisotropy in Faceted Magnetic Nanoparticles Using Biogenic Magnetosomes as a Model. *Nanoscale* **2020**, *12*, 16081−16090.

(27) Marcano, L.; Orue, I.; Gandia, D.; Gandarias, L.; Weigand, M.; Abrudan, R. M.; García-Prieto, A.; García-Arribas, A.; Muela, A.; Fdez-Gubieda, M. L.; Valencia, S. Magnetic Anisotropy of Individual Nanomagnets Embedded in Biological Systems Determined by Axi-Asymmetric X-Ray Transmission Microscopy. *ACS Nano* **2022**, *16*, 7398−7408.

(28) Gandia, D.; Gandarias, L.; Rodrigo, I.; Robles-García, J.; Das, R.; Garaio, E.; García, J. Á.; Phan, M. H.; Srikanth, H.; Orue, I.; Alonso, J.; Muela, A.; Fdez-Gubieda, M. L. Unlocking the Potential of Magnetotactic Bacteria as Magnetic Hyperthermia Agents. *Small* **2019**, *15*, No. 1902626.

(29) Nemati, Z.; Das, R.; Alonso, J.; Clements, E.; Phan, M. H.; Srikanth, H. Iron Oxide Nanospheres and Nanocubes for Magnetic Hyperthermia Therapy: A Comparative Study. *J. Electron. Mater.* **2017**, *46*, 3764−3769.

(30) Das, R.; Alonso, J.; Nemati Porshokouh, Z.; Kalappattil, V.; Torres, D.; Phan, M.-H.; Garaio, E.; García, J. Á.; Sanchez Llamazares,

J. L.; Srikanth, H. Tunable High Aspect Ratio Iron Oxide Nanorods for Enhanced Hyperthermia. *J. Phys. Chem. C* **2016**, *120*, 10086−10093.

(31) Nemati, Z.; Salili, S. M.; Alonso, J.; Ataie, A.; Das, R.; Phan, M. H.; Srikanth, H. Superparamagnetic Iron Oxide Nanodiscs for Hyperthermia Therapy: Does Size Matter? *J. Alloys Compd.* **2017**, *714*, 709−714.

(32) Nemati, Z.; Alonso, J.; Rodrigo, I.; Das, R.; Garaio, E.; García, J. Á.; Orue, I.; Phan, M. H.; Srikanth, H. Improving the Heating Efficiency of Iron Oxide Nanoparticles by Tuning Their Shape and Size. *J. Phys. Chem. C* **2018**, *122*, 2367−2381.

(33) Fratila, R. M.; Rivera-Fernández, S.; De La Fuente, J. M. Shape Matters: Synthesis and Biomedical Applications of High Aspect Ratio Magnetic Nanomaterials. *Nanoscale* **2015**, *7*, 8233−8260.

(34) de Souza Cabral, A.; Verdan, M.; Presciliano, R.; Silveira, F.; Correa, T.; Abreu, F. Large-Scale Cultivation of Magnetotactic Bacteria and the Optimism for Sustainable and Cheap Approaches in Nanotechnology. *Mar Drugs* **2023**, *21*, 60.

(35) Amann, R.; Peplies, J.; Schüler, D.Diversity and Taxonomy of Magnetotactic Bacteria. In *Magnetoreception and Magnetosomes in Bacteria*; Springer: Berlin, Heidelberg, 2006; pp 25−36. .

(36) Le Nagard, L.; Morillo-López, V.; Fradin, C.; Bazylinski, D. A. Growing Magnetotactic Bacteria of the Genus Magnetospirillum: Strains MSR-1, AMB-1 and MS-1. *J. Visualized Exp.* **2018**, *140*, No. e58536.

(37) Lefèvre, C. T.; Bazylinski, D. A. Ecology, Diversity, and Evolution of Magnetotactic Bacteria. *Microbiology and Molecular Biology Reviews* **2013**, *77*, 497−526.

(38) Matsunaga, T.; Sakaguchi, T.; Tadakoro, F. Magnetite Formation by a Magnetic Bacterium Capable of Growing Aerobically. *Appl. Microbiol. Biotechnol.* **1991**, *35*, 651−655.

(39) Schleifer, K. H.; Schüler, D.; Spring, S.; Weizenegger, M.; Amann, R.; Ludwig, W.; Köhler, M. The Genus Magnetospirillum Gen. Nov. Description of Magnetospirillum Gryphiswaldense Sp. Nov. and Transfer of Aquaspirillum Magnetotacticum to Magnetospirillum Magnetotacticum Comb. Nov. *Syst. Appl. Microbiol* **1991**, *14*, 379−385.

(40) Bazylinski, D. A.; Frankel, R. B.; Jannasch, H. W. Anaerobic Magnetite Production by a Marine, Magnetotactic Bacterium. *Nature* **1988**, *334*, 518−519.

(41) Silva, K. T.; Leão, P. E.; Abreu, F.; López, J. A.; Gutarra, M. L.; Farina, M.; Bazylinski, D. A.; Freire, D. M. G.; Lins, U. Optimization of magnetosome Production and Growth by the Magnetotactic Vibrio Magnetovibrio blakemorei Strain MV-1 through a Statistics-Based Experimental Design. *Appl. Environ. Microbiol.* **2013**, *79*, 2823.

(42) Kalirai, S. S.; Bazylinski, D. A.; Hitchcock, A. P. Anomalous Magnetic Orientations of magnetosome Chains in a Magnetotactic Bacterium: Magnetovibrio blakemorei Strain MV-1. *PLoS One* **2013**, *8*, No. e53368.

(43) Jovane, L.; Florindo, F.; Bazylinski, D. A.; Lins, U. Prismatic Magnetite Magnetosomes from Cultivated Magnetovibrio blakemorei Strain MV-1: A Magnetic Fingerprint in Marine Sediments? *Environ. Microbiol Rep* **2012**, *4*, 664−668.

(44) Araujo, A. C. V; Abreu, F.; Silva, K. T.; Bazylinski, D. A.; Lins, U. Magnetotactic Bacteria as Potential Sources of Bioproducts. *Mar Drugs* **2015**, *13*, 389−430.

(45) Zingsem, B. W.; Feggeler, T.; Terwey, A.; Ghaisari, S.; Spoddig, D.; Faivre, D.; Meckenstock, R.; Farle, M.; Winklhofer, M. Biologically Encoded magnonics. *Nat. Commun.* **2019**, *10*, 1−8.

(46) Heyen, U.; Schüler, D. Growth and magnetosome Formation by Microaerophilic Magnetospirillum Strains in an Oxygen-Controlled Fermentor. *Appl. Microbiol. Biotechnol.* **2003**, *61*, 536−544.

(47) Schneider, C. A.; Rasband, W. S.; Eliceiri, K. W. NIH Image to ImageJ: 25 Years of Image Analysis. *Nat. Methods* **2012**, *9*, 671−675.

(48) Marcano, L.; Muñoz, D.; Martín-Rodríguez, R.; Orue, I.; Alonso, J.; García-Prieto, A.; Serrano, A.; Valencia, S.; Abrudan, R.; Fernández Barquín, L.; García-Arribas, A.; Muela, A.; Fdez-Gubieda, M. L. L. Magnetic Study of Co-Doped magnetosome Chains. *J. Phys. Chem. C* **2018**, *122*, 7541−7550.

(49) Carrey, J.; Mehdaoui, B.; Respaud, M. Simple Models for Dynamic Hysteresis Loop Calculations of Magnetic Single-Domain Nanoparticles: Application to Magnetic Hyperthermia Optimization. *J. Appl. Phys.* **2011**, *109*, No. 083921.

(50) Villanueva, D.; Gubieda, A. G.; Gandarias, L.; Abad Díaz de Cerio, A.; Orue, I.; Ángel García, J.; de Cos, D.; Alonso, J.; Fdez-Gubieda, M. L. Heating Efficiency of Different Magnetotactic Bacterial Species: Influence of magnetosome Morphology and Chain Arrangement. *ACS Appl. Mater. Interfaces* **2024**, *16*, 67216−67224.

(51) Walz, F. The Verwey Transition - a Topical Review. *J. Phys.: Condens. Matter* **2002**, *14*, R285−R340.

(52) Verwey, E. J. W. Electronic Conduction of Magnetite (Fe3O4) and Its Transition Point at Low Temperatures. *Nature* **1939**, *144*, 327−328.

(53) García, J.; Subías, G. The Verwey transition—a new perspective. *J. Phys.: Condens. Matter* **2004**, *16*, R145−R178.

(54) Xing, M.; Mohapatra, J.; Elkins, J.; Guragain, D.; Mishra, S. R.; Ping Liu, J. Exchange Bias and Verwey Transition in Fe5C2/Fe3O4 Core/Shell Nanoparticles. *Nanoscale* **2021**, *13*, 15837−15843.

(55) Walz, F. The Verwey Transition - a Topical Review. *J. Phys.: Condens. Matter* **2002**, *14*, R285−R340.

(56) Castellanos-Rubio, I.; Arriortua, O.; Iglesias-Rojas, D.; Barón, A.; Rodrigo, I.; Marcano, L.; Garitaonandia, J. S.; Orue, I.; Fdez-Gubieda, M. L.; Insausti, M. A Milestone in the Chemical Synthesis of Fe3O4 Nanoparticles: Unreported Bulklike Properties Lead to a Remarkable Magnetic Hyperthermia. *Chem. Mater.* **2021**, *33*, 8693−8704.

(57) Řezníček, R.; Chlan, V.; Štěpánková, H.; Novák, P.; Maryško, M. Magnetocrystalline Anisotropy of Magnetite. *J. Phys.: Condens. Matter* **2012**, *24*, No. 055501.

(58) Marcano, L.; García-Prieto, A.; Muñoz, D.; Fernández Barquín, L.; Orue, I.; Alonso, J.; Muela, A.; Fdez-Gubieda, M. L. Influence of the Bacterial Growth Phase on the Magnetic Properties of Magnetosomes Synthesized by Magnetospirillum Gryphiswaldense. *Biochim Biophys Acta Gen Subj* **2017**, *1861*, 1507−1514.

(59) Jefremovas, E. M.; Gandarias, L.; Marcano, L.; Gacía-Prieto, A.; Orue, I.; Muela, A.; Fdez-Gubieda, M. L.; Barquín, L. F.; Alonso, J. Modifying the Magnetic Response of Magnetotactic Bacteria: Incorporation of Gd and Tb Ions into the magnetosome Structure. *Nanoscale Adv.* **2022**, *4*, 2649−2659.

(60) Kim, T.; Sim, S.; Lim, S.; Patino, M. A.; Hong, J.; Lee, J.; Hyeon, T.; Shimakawa, Y.; Lee, S.; Attfield, J. P.; Park, J. G. Slow Oxidation of Magnetite Nanoparticles Elucidates the Limits of the Verwey Transition. *Nat. Commun.* **2021**, *12* (1), 1−12.

(61) Jackson, M. J.; Moskowitz, B. On the Distribution of Verwey Transition Temperatures in Natural Magnetites. *Geophys J. Int.* **2020**, *224*, 1314−1325.

(62) Gorski, C. A.; Scherer, M. M. Determination of Nanoparticulate Magnetite Stoichiometry by Mössbauer Spectroscopy, Acidic Dissolution, and Powder X-Ray Diffraction: A Critical Review. *Am. Mineral.* **2010**, *95*, 1017−1026.

(63) Das, R.; Kalappattil, V.; Phan, M. H.; Srikanth, H. Magnetic Anomalies Associated with Domain Wall Freezing and Coupled Electron Hopping in Magnetite Nanorods. *J. Magn Magn Mater.* **2021**, *522*, No. 167564.

(64) Sahling, S.; Lorenzo, J. E.; Remenyi, G.; Marin, C.; Katkov, V. L.; Osipov, V. A. Heat Capacity Signature of Frustrated Trimerons in Magnetite. *Sci. Rep* **2020**, *10*, 1−6.

(65) Senn, M. S.; Wright, J. P.; Attfield, J. P. Charge Order and Three-Site Distortions in the Verwey Structure of Magnetite. *Nature* **2012**, *481*, 173−176.

(66) Brabers, V.; Walz, F.; Kronmüller, H. Impurity Effects upon the Verwey Transition in Magnetite. *Phys. Rev. B Condens Matter Mater. Phys.* **1998**, *58*, 14163−14166.

(67) Skumryev, V.; Blythe, H. J.; Cullen, J.; Coey, J. M. D. AC Susceptibility of a Magnetite Crystal. *J. Magn Magn Mater.* **1999**, *196*, 515−517.

(68) Kronmüller, H.; Walz, F. Magnetic After-Effects in Fe3O4 and Vacancy-Doped Magnetite. *Philosophical Magazine B* **1980**, *42*, 433−452.

(69) Cullity, B. D.; Graham, C. D. *Introduction to Magnetic Materials* (2nd ed.); John Wiley & Sons 2009; Vol. *12*. .

(70) Boekelheide, Z.; Miller, J. T.; Grüttner, C.; Dennis, C. L. The Effects of Intraparticle Structure and Interparticle Interactions on the Magnetic Hysteresis Loop of Magnetic Nanoparticles. *J. Appl. Phys.* **2019**, *126*, No. 043903.

(71) Ma, Z.; Mohapatra, J.; Wei, K.; Liu, J. P.; Sun, S. Magnetic Nanoparticles: Synthesis, Anisotropy, and Applications. *Chem. Rev.* **2023**, *123*, 3904−3943.

(72) Özdemir, Ö. Coercive Force of Single Crystals of Magnetite at Low Temperatures. *Geophys J. Int.* **2000**, *141*, 351−356.

(73) Abe, K.; Miyamoto, Y.; Chikazumi, S. Magnetocrystalline Anisotropy of Low Temperature Phase of Magnetite. *J. Phys. Soc. Jpn.* **1976**, *41*, 1894−1902.

(74) Özdemir, Ö.; Dunlop, D. J. Low-Temperature Properties of a Single Crystal of Magnetite Oriented along Principal Magnetic Axes. *Earth Planet Sci. Lett.* **1999**, *165*, 229−239.

(75) Barrera, G.; Tiberto, P.; Sciancalepore, C.; Messori, M.; Bondioli, F.; Allia, P. Verwey Transition Temperature Distribution in Magnetic Nanocomposites Containing Polydisperse Magnetite Nanoparticles. *J. Mater. Sci.* **2019**, *54*, 8346−8360.

(76) Goya, G. F.; Berquó, T. S.; Fonseca, F. C.; Morales, M. P. Static and Dynamic Magnetic Properties of Spherical Magnetite Nanoparticles. *J. Appl. Phys.* **2003**, *94*, 3520−3528.

(77) Stoner, E. C.; Wohlfarth, E. P. A Mechanism of Magnetic Hysteresis in Heterogeneous Alloys. *Philos. Trans. R. Soc. A* **1948**, *240*, 599−642.

(78) Bickford, L. R., Jr.; Brownlow, J. M.; Penoyer, R. F. Magnetocrystalline Anisotropy in Cobalt-Substituted Magnetite Single Crystals. *Proceedings of the IEE - Part B: Radio and Electronic Engineering* **1957**, *104*, 238−244.

(79) Muxworthy, A. R.; Williams, W. Critical Superparamagnetic/Single-Domain Grain Sizes in Interacting Magnetite Particles: Implications for magnetosome Crystals. *J. R Soc. Interface* **2009**, *6*, 1207−1212.

(80) Jacobs, I. S.; Bean, C. P. An Approach to Elongated Fine-Particle Magnets. *Phys. Rev.* **1955**, *100*, 1060−1067.

(81) Chikazumi, S. *Physics of Ferromagnetism*, 2nd ed.; Oxford University Press, 2009.

(82) González-Alonso, D.; González, J.; Gavilán, H.; Fock, J.; Zeng, L.; Witte, K.; Bender, P.; Barquín, L. F.; Johansson, C. Revealing a Masked Verwey Transition in Nanoparticles of Coexisting Fe-Oxide Phases. *RSC Adv.* **2021**, *11*, 390−396.